





Thermodynamic and electronic properties of $(\text{Bi}_{1-x}\text{Sb}_x)_2\text{Se}_3$ topological insulator alloy

Tulio Mota ^{*}, Lara K. Teles [†], Filipe Matusalem [‡], and Ivan Guilhon [§]

Grupo de Materiais Semicondutores e Nanotecnologia, Instituto Tecnológico de Aeronáutica (ITA), DCTA, 12228-900 São José dos Campos, Brazil



(Received 16 November 2023; accepted 5 June 2024; published 27 June 2024)

We present a theoretical study of the structural, electronic, and topological properties of the ternary alloy $(\text{Bi}_{1-x}\text{Sb}_x)_2\text{Se}_3$ at the rhombohedral phase through the generalized quasichemical approximation (GQCA) statistical approach and first-principles calculations, including approximate quasiparticle corrections with density functional theory (DFT)-1/2 method. Our results predict good miscibility along the entire composition range. The system exhibits an increase in the inverted energy gap with the increase of the antimony concentration in the alloy. We predict a maximum band gap of 0.28 eV for the Sb concentration $x = 0.7$, as well its variation along the entire alloy composition. The inversion of the atomic orbital character of the valence and conduction band is observed for any considered composition, as well nontrivial \mathbb{Z}_2 topological invariant. The system $(\text{Bi}_{1-x}\text{Sb}_x)_2\text{Se}_3$ is a promising candidate to be a topological insulator without topological phase transition, maintaining its topological order with $\mathbb{Z}_2 = 1$ for the entire alloy composition.

DOI: [10.1103/PhysRevB.109.235150](https://doi.org/10.1103/PhysRevB.109.235150)

I. INTRODUCTION

The interest in topological insulators (TI) has risen in recent years due to their exotic properties, which make them possible platforms for technological applications in quantum computing, spintronics, thermoelectrics, and renewable energy [1,2] due to their robust and special edge and surface states.

One of the challenges for the TI applications in devices is related to the need to increase the bulk band gap of these materials [3]. Thus, mapping new TI candidates has been a challenge for theoretical and experimental research. In this context, alloys that can exhibit topological phase transition [4], as well as maximization of specific electronic properties, and greater flexibility in the choice of materials [5,6], have received much attention in recent years.

Since the discovery of three-dimensional (3D) TI, such as tetradymites of the bismuth telluride family (Bi_2Te_3) with relatively high experimental energy gap, in the order of 0.3 eV, the interest in these materials suffered a significant increase [7]. Thus, other compounds involving these elements or combinations of them in ternary and quaternary systems and alloys have been the subject of different research [8–11].

The first experimental and theoretical studies on the topological properties of alloys already pointed to materials such as $\text{Bi}_{1-x}\text{Sb}_x$ and elevated them to the category of candidates for the realization of “topological insulator materials” [12]. The first two theoretical calculations involving $(\text{Bi}_{1-x}\text{Sb}_x)_2\text{Se}_3$ had as a fundamental purpose the study of

the topological phase transition in this material [13,14]. Both authors agreed that there was a trivial-to-topological transition at $x \approx 0.6$, with the band gap closing at this concentration. Although the phase transition makes sense if one considers the Sb_2Se_3 compound as a conventional insulator (CI), more recent results suggest otherwise [15].

For a long time, several authors classified pure Sb_2Se_3 as a CI [16], highlighting the possibility of topological phase transitions due to pressure [17] and strain [18]. Even later, in recent reviews, Sb_2Se_3 continued to receive the classification of CI, in contrast with other similar tetradymites. However, we have to point out that all these studies considered its most stable crystallographic phase, the so-called stibnite structure [7]. Recently, however, it was shown that the Sb_2Se_3 system exhibits robust TI characteristics in its rhombohedral crystalline structure [15]. It is obvious that, in a sense, inaccurate structural parameters are equivalent to the application of a strain, and therefore, can lead to different and incorrect judgments of the topological class of material under theoretical approaches.

This evidently does not mean that there is an error in previous works that considered the Sb_2Se_3 as a CI, but only predictions for a distinct crystalline phase of this material. Since now the Sb_2Se_3 is found to be a TI in the rhombohedral crystalline phase, we can construct the $(\text{Bi}_{1-x}\text{Sb}_x)_2\text{Se}_3$ alloy using as a basis the structure of the bismuth selenide (Bi_2Se_3) family. In this way, the structure and atomic arrangement remain the same over the entire range of the composition.

In this paper, we present detailed results of the structural properties, electronic structure, and topological order of $(\text{Bi}_{1-x}\text{Sb}_x)_2\text{Se}_3$ alloys in the rhombohedral structure, combining a statistical approach with results from the formalism of density functional theory (DFT), including approximate quasiparticle corrections. We also present results for the topological invariant \mathbb{Z}_2 for the alloy.

^{*}Contact author: tuliomota@ita.br

[†]Contact author: lkteles@ita.br

[‡]Contact author: fmatusalem@ita.br

[§]Contact author: guilhon@ita.br

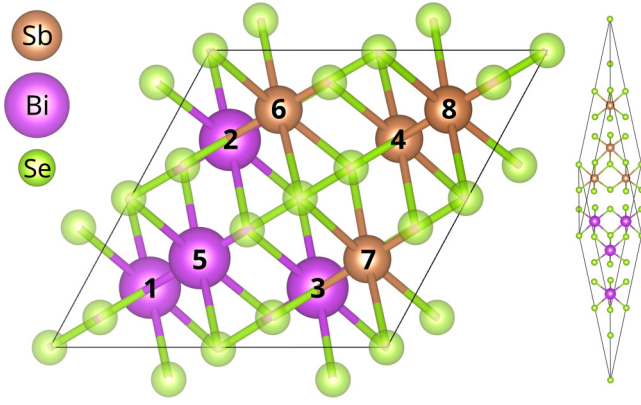


FIG. 1. Illustration of a 3D periodic system for a specific atomic configuration, class $j = 11$. In this supercell, the atomic sites are represented by labels 1,2,3,...,8. Consequently, we adopted “BBB-SBSSS” to describe this configuration, considering B to represent Bi atoms and S to represent Sb atoms.

II. METHODOLOGY

A. Generalized quasichemical approximation

Dealing with nonperiodic systems and also with random ordering can be a hard task for first-principles calculations based on the density functional theory (DFT) [19,20], when periodic boundary conditions are used. This circumstance can limit the correct description of alloys. To overcome this problem, we use the generalized quasichemical approximation (GQCA) [21] a formalism able to do a statistical treatment of the results obtained from the DFT. In summary, the alloy can be described by an individual arrangement of energetically independent clusters. GQCA makes it possible to determine thermodynamic properties, excess properties, phase decomposition, and electronic properties for the entire alloy composition. Within this method, each independent cluster j with a specific number of Bi and Sb atoms is associated with a probability x_j .

The clusters that represent $(\text{Bi}_{1-x}\text{Sb}_x)_2\text{Se}_3$ are defined from the expansion in supercells of $2 \times 2 \times 1$ of the bismuth selenide unit cell, as shown in Fig. 1 and their appropriate labels. A total of 34 different possible configurations for the clusters are taken into account and are listed in Table I. These cluster classes and their degeneracy g_j are sufficient to encompass all possible combinations for the positions of Bi and Sb atoms in the supercell.

The excess energy $\Delta\varepsilon_j$ is calculated to evaluate the relative stability of the alloy for each cluster formation j :

$$\Delta\varepsilon_j = \varepsilon_j - \frac{n_j}{n}\varepsilon_{34} - \left(1 - \frac{n_j}{n}\right)\varepsilon_1, \quad (1)$$

where $n = 8$ is the number of atoms belonging to group 5A in each cluster and ε_1 and ε_{34} are the total energies of the cluster configurations relative to Bi_2Se_3 and Sb_2Se_3 , respectively.

To determine the probability that an individual cluster $x_j(x, T)$ belongs to the class j , where $j = 1, 2, \dots, J$ for an average alloy composition x in a temperature T , we have [22]

$$x_j(x, T) = \frac{g_j \lambda^{n_j} \exp(-\beta \Delta\varepsilon_j)}{\sum_{j=0}^J g_j \lambda^{n_j} \exp(-\beta \Delta\varepsilon_j)}, \quad (2)$$

TABLE I. The 34 different classes of 20-atom supercell clusters for 3D alloy study. Table constructed based on the “Sb atoms” column. Labels for the sites occupied by Sb atoms in the cluster can be found in Fig. 1.

j	n_j	g_j	Sb atoms	j	n_j	g_j	Sb atoms
1	0	1	—	18	4	4	8,7,4,3
2	1	8	8	19	4	8	8,6,4,3
3	2	8	8,7	20	4	16	8,5,4,3
4	2	4	8,5	21	5	16	8,7,6,4,3
5	3	8	8,7,6	22	4	4	8,6,3,1
6	4	2	8,7,6,5	23	5	16	8,6,5,4,3
7	2	4	8,4	24	6	8	8,7,6,5,4,3
8	2	8	8,3	25	4	2	8,5,4,1
9	3	16	8,7,4	26	5	8	8,7,5,4,1
10	3	8	8,5,3	27	4	2	8,5,3,2
11	4	8	8,7,6,4	28	5	8	8,7,5,3,2
12	2	4	8,1	29	6	4	8,7,6,5,3,2
13	3	8	8,5,4	30	6	4	8,7,6,4,3,2
14	3	16	8,6,3	31	6	8	8,7,5,4,3,2
15	4	16	8,7,5,4	32	6	4	8,6,5,4,3,1
16	4	8	8,6,5,3	33	7	8	8,7,6,5,4,3,2
17	5	8	8,7,6,5,4	34	8	1	8,7,6,5,4,3,2,1

for which $\beta = 1/kT$, with k the Boltzmann constant, and the factor λ is determined from the average composition. This expression is determined by minimizing the mixing free energy of the alloy system with two conditions [23], the first associated with a normalization condition

$$\sum_{j=1}^N x_j(x, T) = 1, \quad (3)$$

and the second to the concentration of Bi in the alloy

$$\sum_{j=1}^N n_j x_j(x, T) = nx. \quad (4)$$

It is possible to map certain properties of the alloy $p(x, T)$ through an average of the values of this property p_j weighted by the occurrence probabilities $x_j(x, T)$,

$$p(x, T) = \sum_{j=0}^J x_j(x, T) P_j, \quad (5)$$

where P_j is the arbitrary property of each j cluster class.

The composition fluctuation effects can be estimated by considering mean-squared deviations around the average value for a given property

$$\Delta p(x, T) = \sqrt{\sum_{j=0}^J x_j P_j^2 - \left(\sum_{j=0}^J x_j P_j\right)^2}. \quad (6)$$

As each cluster configuration j can be considered individually as an infinite and periodic system, its physical properties can be calculated via DFT individually. For more details, the formalism of the GQCA method and the cluster expansion approach are extensively discussed elsewhere [21–24].

B. DFT and DFT-1/2 method

Although the DFT is quite successful in describing a large set of properties, this is not true for the band gap of conventional semiconductors, which is usually underestimated [25]. In the case of topological insulators, due to the inversion of the orbital character of the bands, there is an overestimation of the gap [26]. Thus, a correct description of the topological character of the systems requires a reliable band structure of the material.

This problem can lead to false-positive or false-negative signatures of topological order [27]. To overcome this problem we use the DFT-1/2 method, which successfully describes the electronic properties of alloys, two-dimensional (2D), and 3D materials [28,29]. Furthermore, its low computational cost is an essential factor since the present work deals with 34 calculations of individual clusters, where the inclusion of spin-orbit coupling (SOC) is mandatory.

Since we are dealing with topological insulators in all clusters of the alloy, all configurations receive individual DFT-1/2 corrections, following the procedures and specificities described in Ref. [30].

In DFT-1/2 the formalism of the one-particle Kohn-Sham equation becomes

$$\left[-\frac{1}{2}\nabla^2 + V_{\text{KS}}(\vec{r}) + \tilde{V}_s(\vec{r}) \right] \phi_i(\vec{r}) = \epsilon_i \phi_i(\vec{r}), \quad (7)$$

where \tilde{V}_s is the DFT-1/2 correction potential.

The only parameter to be determined in DFT-1/2 is related to a cutoff function $\Theta(r)$, which exists to adjust the potential \tilde{V}_s , in the form $\tilde{V}_s = \Theta(r)V_s(r)$, thus avoiding self-energy interactions at neighboring atom sites

$$\Theta(r) = \begin{cases} A \left[1 - \left(\frac{r}{\text{CUT}} \right)^8 \right]^3 & \text{if } r \leq \text{CUT}, \\ 0 & \text{if } r \geq \text{CUT}, \end{cases} \quad (8)$$

where A is a constant and represents the correction amplitude. In the context of topological insulators, we are in a state of inverted bands, so we take A as -1 (minus one) since the correction is performed using the valence band as a reference.

More details regarding the formalism and implementation of DFT-1/2 are widely discussed elsewhere [31,32].

In the analyzes regarding the changes provided by the DFT-1/2 over the standard DFT, we observe how the degree of inversion remains (or not) in the clusters despite the change in the gaps and energy levels. Calculating the band inversion level by observing the last occupied band for each cluster class as follows:

$$\eta_{\text{inv}}(\vec{k}) = N \cdot [\zeta_{\text{inv}}(\vec{k})/\zeta_M]^2, \quad (9)$$

where N is a normalization factor and $\zeta_{\text{inv}}(\vec{k})$ is the orbital contribution of the p orbital in the formation of the valence band that is inverted.

C. Computational details

The *ab initio* calculations based on the density functional theory formalism are performed using the Vienna Ab initio Simulation Package (VASP) code. The exchange-correlation functional (XC) was treated within the Perdew-Burke-Ernzerhof [33], in the generalized gradient approximation (GGA-PBE), and in this work it is also called the ‘‘standard DFT.’’ To obtain the convergence of the complete system

the relaxation of the atomic coordinates of the unit cell is carried out until the forces are less than 0.001 eV/Å. In all self-consistent calculations (DFT GGA and DFT-1/2) a $6 \times 6 \times 6$ Γ -centered k -point mesh is employed. The adopted energy cutoff for the plane-wave expansions was 400 eV. The Kohn-Sham formalism is solved using the projector augmented-wave (PAW) scheme [34,35].

Although the pure Bi_2Se_3 and Sb_2Se_3 systems exhibit spatial inversion symmetry, expanding the unit cell of these systems to represent individual alloy clusters, with their intermediate concentrations, removes the symmetry from the system. Thus generalized methods for determining the topological invariant \mathbb{Z}_2 are needed.

To obtain topological invariant results for the 34 different cluster configurations, the Z2PACK software package [36,37] implemented in VASP code was used. This package builds on results from the WANNIER90 package to generate Wannier functions (WFs) from the outputs of the DFT calculation [38], where it can generate maximally localized WFs and provide Wannier charge centers (WCC) [39,40]. For the formal determination of the Wannier function centers [41] scripts were used to calculate the evolution of the WCC [30,42].

III. RESULTS AND DISCUSSION

For all cluster configurations, we consider the crystalline structure of the Bi_2Se_3 family, i.e., binary tetradymites compounds, e.g., Bi_2Te_3 and Sb_2Te_3 , which has a rhombohedral primitive cell, with a hexagonal unit cell, belonging to the space group $D_{3d}^5(R\bar{3}m)$ [43]. This system is organized in quintuple layers (QL) with two inequivalent Se sites in the form $\text{Se}_1\text{-Bi-}\text{Se}_2\text{-Bi-}\text{Se}_1$.

Caution is needed when analyzing the synthesis of the system $(\text{Bi}_{1-x}\text{Sb}_x)_2\text{Se}_3$, especially in concentrations with a predominance of Sb, which is an analog to the synthesis of the Sb_2Se_3 rhombohedral phase [44,45]. Despite this issue, a detailed theoretical investigation through DFT and molecular dynamics calculations of Sb_2Se_3 in a rhombohedral structure confirms that it is both energetically and kinetically stable at finite temperatures [15]. Recently, experimental work was successful in growing rhombohedral Sb_2Se_3 for an ultrathin film. Although they did not identify signatures of the non-trivial topology of Sb_2Se_3 , the authors highlighted that the main possibility of making Sb_2Se_3 a topological insulator is to choose an appropriate substrate, capable of overcoming ‘‘the orthorhombic phase issue’’ [46].

Before these works, thin films of $(\text{Bi}_{1-x}\text{Sb}_x)_2\text{Se}_3$ were also prepared showing the coexistence of the rhombohedral and orthorhombic in the alloy at specific concentrations in which the rhombohedral phase was considered stable for x up to 0.5 [47]. However, other work demonstrated the successful growth of molecular beam epitaxy (MBE) of rhombohedral thin films of $(\text{Bi}_{1-x}\text{Sb}_x)_2\text{Se}_3$ with high concentrations of Sb (with high x up to 0.8) [45]. From an experimental standpoint, the synthesis of a rhombohedral $(\text{Bi}_{1-x}\text{Sb}_x)_2\text{Se}_3$ phase in the entire range of compositions might be induced by the choice of favored substrate, strain, or appropriate experimental techniques. However, this problem is still an open question.

We would also like to emphasize that the methodology adopted in this paper, the GQCA, requires the same atomic

TABLE II. Equilibrium lattice parameters a and c of the supercell used in the alloy for the 34 clusters configurations.

j	a (Å)	c (Å)	j	a (Å)	c (Å)
1	4.143	28.636	18	3.975	27.880
2	4.117	28.445	19	4.040	27.879
3	4.069	28.262	20	4.007	27.901
4	4.091	28.278	21	3.979	27.698
5	4.065	28.081	22	4.039	27.920
6	4.039	27.920	23	4.016	27.720
7	4.091	28.250	24	3.949	27.538
8	4.103	28.263	25	4.039	27.920
9	4.037	28.065	26	4.048	27.741
10	4.040	28.099	27	4.039	27.920
11	4.040	27.882	28	3.977	27.741
12	4.091	28.278	29	3.988	27.562
13	4.076	27.919	30	3.999	27.369
14	4.069	28.080	31	3.947	27.541
15	4.005	27.902	32	3.988	27.562
16	4.045	27.920	33	3.962	27.359
17	4.014	27.720	34	3.936	27.204

arrangement for all the cluster configurations. Therefore, a comparison between rhombohedral and stibnite/orthorhombic (or coexistence of these phases) demands another thermodynamic framework and goes beyond this work. However, experimental results indicated that this synthesis could be, in principle, achieved under proper conditions and the presented. Thus, the presented formalism is valid for any $(\text{Bi}_{1-x}\text{Sb}_x)_2\text{Se}_3$ alloy in its rhombohedral phase.

For pure Bi_2Se_3 ($j = 1$), we identified $a = 4.143$ Å and $c = 28.636$ Å, values equal to or very close to experimental [48,49], and theoretical results [50,51]. For the other pure compound, Sb_2Se_3 ($j = 34$), the lattice parameters are also reasonable, we obtain $a = 3.936$ Å and $c = 27.204$ Å, a difference less than 2% when compared to another theoretical result [18]. The lattice parameters a and c are in broad agreement with other references and experimental results. The lattice parameter for the other 32 atomic arrangements with intermediary compositions stands between values calculated for the end components. The lattice constants of these and other configurations are listed in Table II.

As the presence of Sb atoms increases in the class of individual clusters, a reduction in the lattice constants of that configuration is observed. Nevertheless, the parameters a and c of the hexagonal cell continue to show good agreement with other theoretical results when comparing configurations with an intermediate or predominant presence of Sb in the cluster with results from other works on the pure Sb_2Se_3 [15,17,18,43,52]. These cited works show that depending on the chosen XC functional and whether or not the van der Waals interaction (vdW) is included, the lattice parameters can vary widely for a in Sb_2Se_3 ranging from 3.99 [18] to 4.10 Å [15], and $c = 27.56$ [18] to 30.56 Å [15] (see on the right axis of Fig. 2), thus becoming similar to those of Bi_2Se_3 .

For a detailed result of the structural properties of all configurations Fig. 2 depicts all individual parameters of each

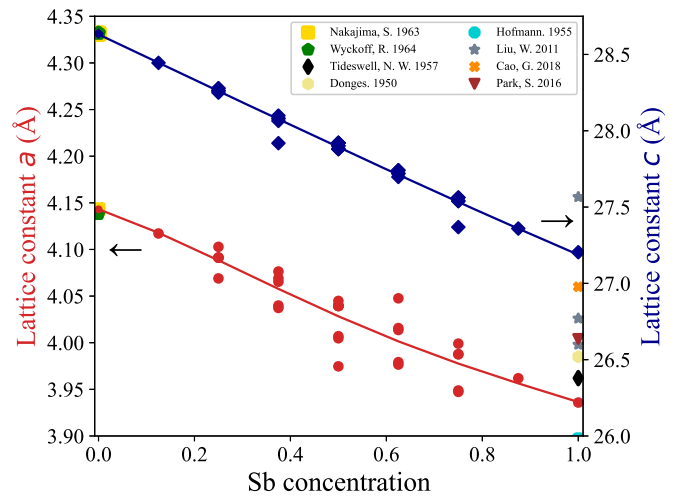


FIG. 2. Lattice parameters a and c of $(\text{Bi}_x\text{Sb}_{1-x})_2\text{Se}_3$ alloy as a function of Sb concentration in the alloy, compared with experimental data. The scatter symbols (circle and diamond) represent data from an individual cluster and its composition.

calculated cluster class and its trend lines, in comparison with results from other works and experimental results.

The most favorable specific cluster atomic configurations are determined by the thermodynamics of the alloy in the GQCA. Thereby, the plot of excess energies ($\Delta\epsilon_j$) of the 34 cluster classes as a function of Sb concentration is depicted in Fig. 3. The excess energies show that all configurations representing mixtures have negative energies, and must therefore be stable against phase separation into pure compounds. As can be seen in Fig. 3, there are two classes of configurations ($j = 18$ and $j = 27$) with more negative values with composition equal to 50%. The most negative one, $j = 27$, presents a configuration that is very symmetrical, where the elements Bi and Sb are stacked in groups of three atoms (see Fig. 4) and in the quintuple layers these elements appear alternately in the pnictogens layer.

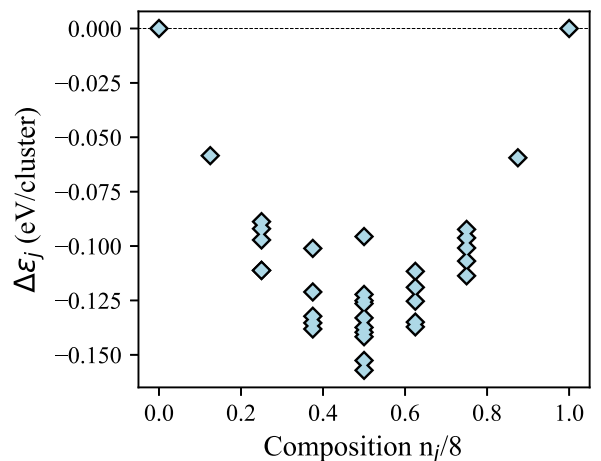


FIG. 3. The thermodynamic stability of the system can be evaluated through the excess energies of the alloy ($\Delta\epsilon_j$) [presented in Eq. (1)], for each configuration $(\text{Bi}_{8-n_j}\text{Sb}_{n_j})\text{Se}$.

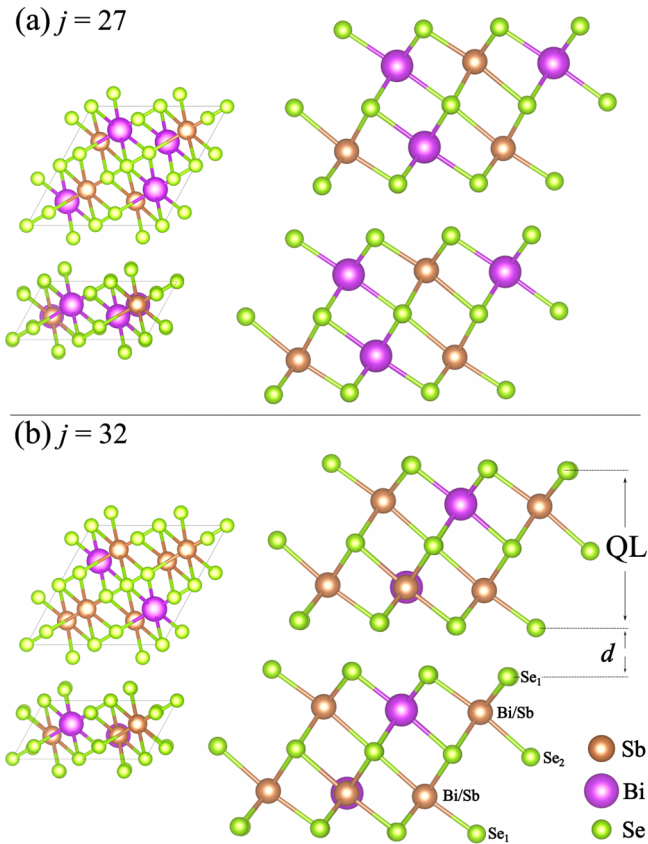


FIG. 4. Optimized crystal structures of special clusters in the alloy in different views of the primitive cell. In (a) the class $j = 27$ is considered the most thermodynamically stable according to the results of the GQCA approach. In (b) the class $j = 32$ is the one that maximizes the inverted band gap from the DFT-1/2 method. We highlight the formation of the QL and their interlayer distances d .

We did not identify classes of configurations for the alloy that are energetically unfavorable and our results indicate easy miscibility since the calculated excess energies are negative for the entire composition range.

In the case of the electronic properties of the alloy, the results of the standard DFT indicate that the majority (more than 95%) of the cluster configurations have an indirect gap, in which the valence band of these systems takes an “*M*-shape, also known as the “Mexican hat,” in the center of the Brillouin zone. We find that the average band gap of these configurations is 0.33 eV. However, as we emphasize that the quasiparticle correction is essential for these systems, when we apply the DFT-1/2 we obtained several changes in the indirect (direct) gap determination, in the shape of the valence and conduction bands, and also the energy gap.

The electronic band structures of the standard DFT show that the projected bands on the atoms for all systems have the Se states forming the last occupied bands. The p -Se states dominate the valence band (except in the inversion regions) and the other occupied bands (by more than 75% of the calculated orbital character of crystalline states), in any alloy composition. The DFT-1/2 method considers the orbital composition of the valence band maximum (VBM) and of the conduction band minimum (CBM) to define the degree

TABLE III. DFT-1/2 cutoff radius (CUT) calculated in this work considering a complete correction for the level of valence and conduction associated with the inverted gap of the topological insulators. In addition to the pure systems Bi_2Se_3 and Sb_2Se_3 , the intermediate classes $j = 2$ to $j = 33$ are listed and include the CUT parameter for the three atomic species. The distance of the first neighbors of the same atomic species is also listed (d).

Material	Class j		CUT (a.u.)	d (Å)
Bi_2Se_3	1	Bi	3.00	4.14
		Se	1.25	3.48
		Bi	3.00	-
$(\text{Bi}_{1-x}\text{Sb}_x)_2\text{Se}_3$	2 to 33	Sb	4.00	-
		Se	1.25	-
		Sb	4.00	3.93
Sb_2Se_3	34	Se	1.25	3.18

of correction for each orbital. However, for TI systems this region has an inverted orbital character. In this region, the p -Bi states dominate with more than 60% when it is a majority composition of Bi in the cluster, while in compositions where Sb predominates, the presence of p -Sb is also observed with a contribution of 50% to 60% on band formation. As expected, in intermediate compositions of Bi and Sb, the contributions are divided by the p orbitals of the three elements, in addition to s -Se.

In the Table III we list the obtained DFT-1/2 cutoff parameters (CUT) of all calculated cluster classes. We detail that for all the configurations the transferability of this parameter to the atomic species was adopted, that is, in the intermediate configurations ($j = 2$ to $j = 33$) we always take fixed CUTs. Furthermore, the few differences in the orbital character of the bands of these configurations allowed us to construct a unique correction potentials for all clusters.

The band structures calculated via DFT-1/2 presented several differences in comparison with the standard DFT one. Beyond the change in the band-gap size, a change in the type of transition from indirect to direct was observed in 35% of the configuration classes. The direct-to-indirect transition also occurs in a single class ($j = 12$). As expected, in all configurations there was a reduction of the fundamental gap with the inclusion of the quasiparticle correction, as expected since, for topological insulators, the character of the bands is inverted. Furthermore, close to the Γ point, the region where the band inversion takes place, the shape of the conduction band minimum (CBM), and the valence band maximum (VBM) undergoes more pronounced changes, in comparison with other regions of the BZ.

In Fig. 5 we show four cluster configurations and their respective electronic bands, highlighting the comparison between DFT-1/2 and DFT results. It is notable how the *M*-shape of the VBM is swept and the band assumes a parabolic-like format, even with an indirect gap as in the case of class $j = 2$, as depicted in Fig. 5(a). For the pure compound Bi_2Se_3 , this type of behavior has already been widely discussed in other theoretical [30,52–54] and experimental [55] works. This type of behavior, generally observed in materials of this type, is a direct consequence of the band inversion due to spin-orbit interactions and the subsequent applications of

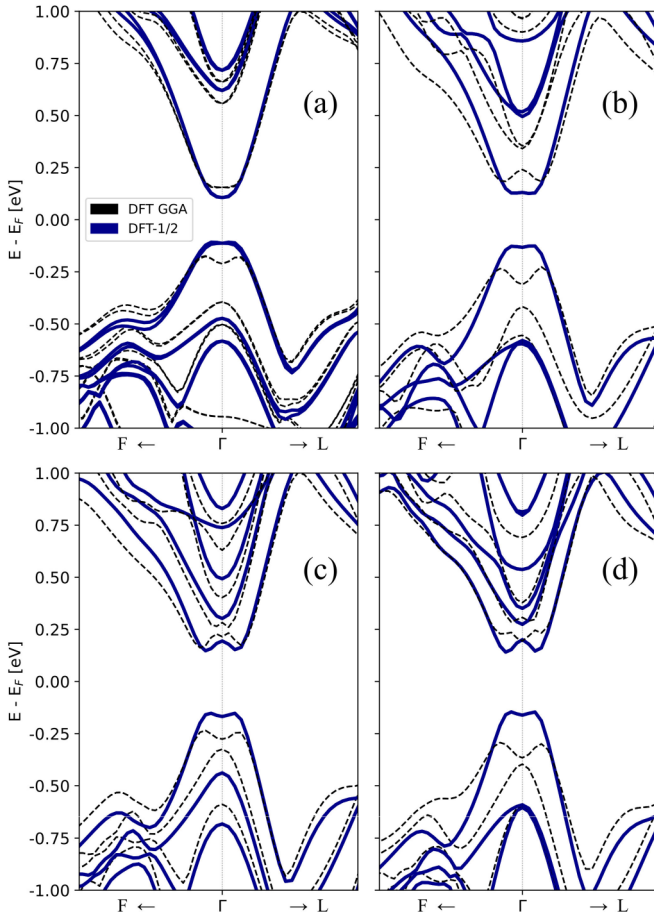


FIG. 5. Electronic band structure with SOC, a comparison between DFT (black dotted line), and DFT-1/2 (solid blue line), for different classes of clusters, in (a) class $j = 2$, (b) $j = 22$, (c) $j = 30$, and (d) $j = 32$.

corrections to the DFT. This effect was extensively investigated and originally illustrated using models with the $k \cdot p$ Hamiltonian for the Bi_2Se_3 -family [43,56]. However, this result is new to intermediary concentrations of the alloy.

This behavior also happens in all other 30 configurations, where an average reduction of 0.07 eV in the fundamental gap and significant changes in the shape of the bands around the Γ point are observed.

We also analyzed the orbital projected bands for the 34 different configurations. We highlight in Fig. 6 two configurations, $j = 25$ and $j = 34$, with clear changes in the format and character of VBM and CBM. In DFT results it is already possible to notice the inversion of the character of the bands around the Γ point, with the Se- p orbital giving place to the Sb- p orbital. However, this intrinsic property of the TI becomes even more significant after the correction provided by the DFT-1/2. While in the class configuration $j = 34$ the inversion in the conduction band occurs at a level with more energy than the CBM (still at the Γ point) in the DFT-1/2 the inversion is clearer and present in CBM around Γ .

For the $j = 25$ class, the inversion is also more evident from a simpler behavior of the bands at k -points around the VBM and CBM, where there is a detachment of the occupied

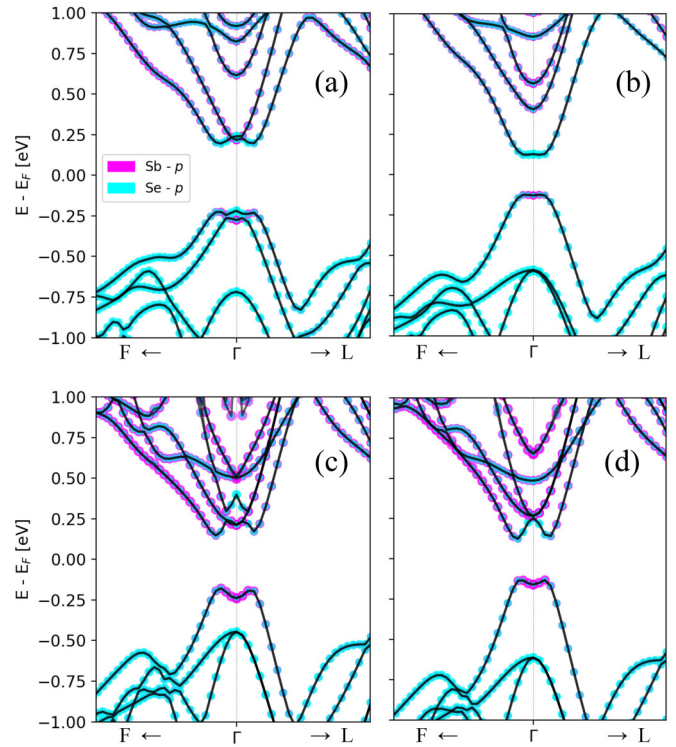


FIG. 6. Electronic band structure with orbitals projections, a comparison between DFT and DFT-1/2. Colors are proportional to the p -states of Sb (magenta) and Se (cyan). For system $j = 25$: (a) DFT GGA and (b) DFT-1/2, for system $j = 34$ (equivalent to pure Sb_2Se_3): (c) DFT GGA and (d) DFT-1/2.

band lower than the VBM and also from more energetic unoccupied bands.

We can see, comparing the Figs. 6(a) and 6(c) with Figs. 6(b) and 6(d) a detachment of the bands forming both the VBM and CBM, after the inclusion of the DFT-1/2 correction. In Fig. 6(a) both VBM and CBM are formed by the crossings of two bands, but becomes single band formed after the inclusion of the DFT-1/2 correction, as we can see in Fig. 6(c). It happens due to the inverted character of the bands around Γ . While Se- p -like parts of the bands are pulled down in the energy scale the Sb- p -like ones are pushed in the opposite direction. This behavior is an intrinsic characteristic of the DFT-1/2 method that was conceived to reduce the self-interaction energy that consequently pulls down in the energy scale the states belonging to the VBM and pushes up the states belonging to the CBM.

One of the desirable results for 3D topological insulators is that they have large band gaps. To enable technological applications at higher temperatures. Figure 7 depicts the curve of this property provided by GQCA. We compare the gap results of the DFT and those provided by the DFT-1/2 correction. The curves are described as a function of the antimony concentration at room temperature (300 K).

The Sb concentration for which the gaps are maximum is shown in Fig. 7. This result is calculated through a statistical average of individual energy gaps E_{g_j} of individual clusters, as described in the methodology section. While DFT predicts a maximum gap of around 57% of Sb, the DFT-1/2 correction

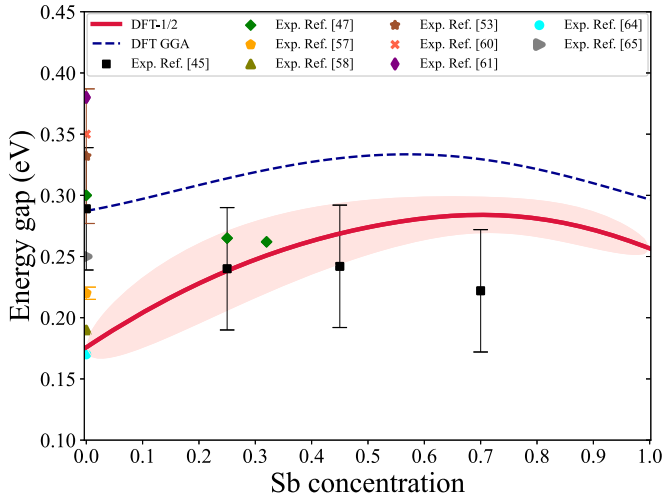


FIG. 7. Comparison between the energy gaps of the alloy in the two approaches, the standard DFT (blue dashed line) and DFT-1/2 (red solid line) and respective mean-square deviation (shaded region) at room temperature. The maximum points are 57% in antimony concentration for the standard DFT and 70% in the DFT-1/2. Symbols in other colors and markers represent available experimental data for $x = 0.0, 0.25, 0.32, 0.45$, and 0.70 [45,47,53,57–65].

defines a maximum gap for a concentration of Sb of 70%. We also verified this behavior in a wide range of higher temperatures. Nevertheless, as there is a random alloy behavior, there are no significant differences considering temperatures greater than 100 K, according to our model.

Bi_2Se_3 is reported with experimental results of 0.17–0.38 eV [53,57–65], also compatible with *ab initio* results including GW of 0.19 eV [53], which, in turn, are very close to the band gap calculated via DFT-1/2 of 0.18 eV. For Sb_2Se_3 , in the same structure as the present work, a band-gap result of ~ 0.17 eV through the GW was reported [44] and 0.18 eV via the optB86b-vdW functional [15]. These results are compatible with our results from DFT-1/2 of 0.25 eV for this system. Figure 7 illustrates the statistical average, obtained through GQCA, of the fundamental energy gap E_g and its root mean square deviations (ΔE_g) calculated via DFT and DFT-1/2, compared with the experimental data for the alloy $(\text{Bi}_{1-x}\text{Sb}_x)_2\text{Se}_3$. The lines represent the theoretical results and the light red shaded area indicates the rms of the calculations. A good correspondence of the DFT-1/2 results with experimental data for intermediate Sb concentrations is observed, indicating an improvement over the pure DFT results. The experimental data are marked with colored symbols corresponding to different references and show ARPES measurements with dispersions up to 0.1 eV, a considerable value given the generally low values of their gaps. For Sb concentrations of 0.25, 0.45, and 0.70, the measured gaps range from 0.22 eV to 0.28 eV, while DFT-1/2 calculations present values of 0.24 eV, 0.26 eV, and 0.28 eV, respectively. Additionally, for the pure compound Bi_2Se_3 , there is a wide variation in experimental data, ranging from 0.17 eV to 0.38 eV. This analysis demonstrates that despite the large uncertainties in experimental measurements, the DFT-1/2 correction results are in satisfactory agreement

TABLE IV. Bowing parameter b according to the expression $E_g(x) = E_g^1x + E_g^0(1-x) - bx(1-x)$, and the maximum gaps E_g between cluster configurations for the two approaches used.

	$(\text{Bi}_{1-x}\text{Sb}_x)_2\text{Se}_3$	
	DFT GGA	DFT-1/2
Bowing parameter b	−0.17 eV	−0.23 eV
Maximum E_g	0.383 eV	0.313 eV

with the available experimental data, with all calculated values falling within the experimental range. We estimated a bowing parameter (b) for the energy gap dependency with composition for DFT and DFT-1/2, considering the expression present in Table IV.

We highlight the two classes of special configurations, $j = 27$ and $j = 32$, for which the gap is maximum according to the DFT-1/2, in Fig. 4, where two views of the primitive cell of these configurations are presented.

Also, a detailed record of all calculated fundamental gaps for all 34 cluster configurations from DFT-1/2 and DFT is presented in Table V. In addition, the table also contains the excess energies calculated through Eq. (1).

To investigate the importance of these completely relativistic calculations for the alloy, we compared the results calculated for all the individual clusters without considering the SOC, and then the gap curve for the alloy at room temperature and higher temperatures (see Fig. 1 in the Supplemental Material Ref. [66]). It is clear that when the SOC is turned off, there are strong changes in the band-gap values. For some concentrations, such as 25% Sb in the alloy, the gap is close to 0 eV, and additionally, the band gap becomes direct for all classes of clusters. Furthermore, it is notable that there is an opposite behavior (practically inverted) in the gap curve without SOC both when comparing DFT-1/2 and standard DFT, both with SOC. Something that was already expected since the strong spin-orbit interaction for heavier elements, and in particular, for these specific materials [54,67], plays a fundamental role in the determination of electronic properties.

Determining topological invariants can be computationally expensive depending on the complexity of the material and chosen approach. In addition, the mandatory inclusion of the SOC, the number of cluster configurations of the alloy (34), and the spatial inversion symmetry breaking that naturally occurs in certain individual clusters make it difficult to determine the topological invariant \mathbb{Z}_2 .

We determine the \mathbb{Z}_2 invariant through the Wannier functions (WF) methodology, in which the evolution of the charge centers of the WF through a direction in the BZ are taken into account in the determination of the topological invariant [41]. The WF functions are first constructed from the DFT wave function in such a way as to correctly represent the Hamiltonian of the system.

Figure 8 depicts a comparison between the band structure results from standard DFT calculations and WFs for the class $j = 13$, where a good agreement is observed, confirming that the representation of the system in the WF space is satisfactory.

TABLE V. Energy gap from DFT GGA ($E_{g_j}^{\text{GGA}}$), DFT-1/2 ($E_{g_j}^{\text{DFT-1/2}}$) approach (in eV), excess energy $\Delta\varepsilon_j$ (eV), and degeneracies (g_j) of cluster configurations $(\text{Bi}_{1-x}\text{Sb}_x)_2\text{Se}_3$.

$(\text{Bi}_{1-x}\text{Sb}_x)_2\text{Se}_3$									
Class j	$\Delta\varepsilon_j$	g_j	$E_{g_j}^{\text{GGA}}$	$E_{g_j}^{\text{DFT-1/2}}$	Class j	$\Delta\varepsilon_j$	g_j	$E_{g_j}^{\text{GGA}}$	$E_{g_j}^{\text{DFT-1/2}}$
1	0.0	1	0.2873	0.1758	18	-0.1525	4	0.3210	0.2690
2	-0.0584	8	0.2975	0.2138	19	-0.1374	8	0.3319	0.2880
3	-0.0887	8	0.3045	0.2305	20	-0.1416	16	0.3448	0.2849
4	-0.0920	4	0.3220	0.2251	21	-0.1349	16	0.3341	0.2830
5	-0.1010	8	0.3219	0.2394	22	-0.1222	4	0.3605	0.2523
6	-0.0956	2	0.3230	0.2450	23	-0.1189	16	0.3399	0.2957
7	-0.1111	4	0.3094	0.2372	24	-0.0962	8	0.3228	0.2805
8	-0.1112	8	0.3144	0.2512	25	-0.1330	2	0.3830	0.2486
9	-0.1353	16	0.3139	0.2553	26	-0.1253	8	0.3590	0.3042
10	-0.1381	8	0.3313	0.2569	27	-0.1571	2	0.3449	0.2740
11	-0.1396	8	0.3222	0.2583	28	-0.1371	8	0.3422	0.2883
12	-0.0971	4	0.3454	0.2773	29	-0.1008	4	0.3358	0.2843
13	-0.1322	8	0.3410	0.2880	30	-0.1136	4	0.3206	0.2998
14	-0.1210	16	0.3399	0.2861	31	-0.1068	8	0.3364	0.2979
15	-0.1264	16	0.3438	0.2811	32	-0.0923	4	0.3420	0.3139
16	-0.1251	8	0.3405	0.2845	33	-0.0594	8	0.3135	0.2781
17	-0.1116	8	0.3342	0.2756	34	0.0	1	0.2966	0.2567

The \mathbb{Z}_2 result for class $j = 34$, equivalent to pure Sb_2Se_3 , is depicted in Fig. 9. In this methodology, the determination of the trivial or topological character of the material is made by drawing an arbitrary reference line parallel to the horizontal axis and observing if the number of crossings of this line in the centers of the WFs is odd or even. An odd number of crossings characterizes topological insulator materials. In this way, the class $j = 34$ has a nontrivial topological order since it has a single crossing in the plane $k_z = 0$ and a crossing equal to zero in the plane $k_z = 1$. We highlight one of the classes in the figure, however, the result of this invariant is the same for the other 33 different classes (see Supplemental Material Ref.

[66]). The results indicated by the WCC dispersion are the same, which shows the robustness of the topological order of this family of alloys in any considered concentration and in the different atomic arrangements of the individual clusters.

To further evaluate the differences between DFT results and the DFT-1/2 correction regarding orbital character in the valence band, we calculate the level of band inversion for the 34 cluster configurations. In Fig. 10 some results of this degree of inversion are shown for five specific classes ($j = 5, 13, 22, 25$, and 26). For most classes, the results are quite similar to those shown for classes $j = 5$ and $j = 22$, where there is a peak and a narrowing of the inversion level around the Γ point when the DFT-1/2 is applied; a result that is similar for both methodologies most of the time. For the classes $j = 13, j = 25$, and $j = 26$ the DFT calculations result in two peaks forming a kind of *M-shape* around Γ . However, after the inclusion of the DFT-1/2 correction only one peak appears. This change occurs due to the different degree of contribution of each orbital forming the band in a function of the distance to the Γ point, i.e., the two peaks region has a lower concentration of the Sb-*p* like orbital than the valley at Γ , resulting in the valley being pushed higher in energy than the peaks. The inverse behavior also occurs in the CBM.

Since we know that the pure end components of the alloy are TI, and after the approximate quasiparticle correction calculation with DFT-1/2 as well as the calculation of the topological invariant \mathbb{Z}_2 show all 34 clusters considered to be TI, the results represent strong evidence that the topological properties of this family of alloys are quite robust in terms of atomic arrangement and chemical concentration. Thus, these considerations combined with the thermodynamic results clearly indicate that a TI-CI phase transition should not occur in the $(\text{Bi}_{1-x}\text{Sb}_x)_2\text{Se}_3$ alloy.

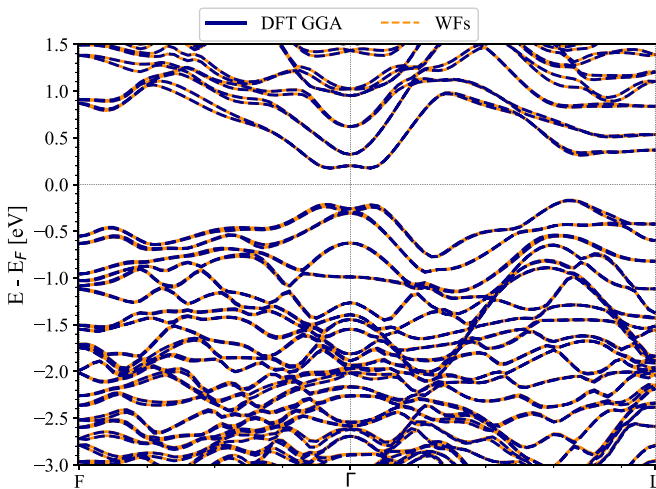


FIG. 8. Band structure of an individual alloy cluster, class $j = 13$, comparing that obtained in a DFT calculation (blue solid line) with that obtained from Wannier functions (WFs) (orange dashed line).

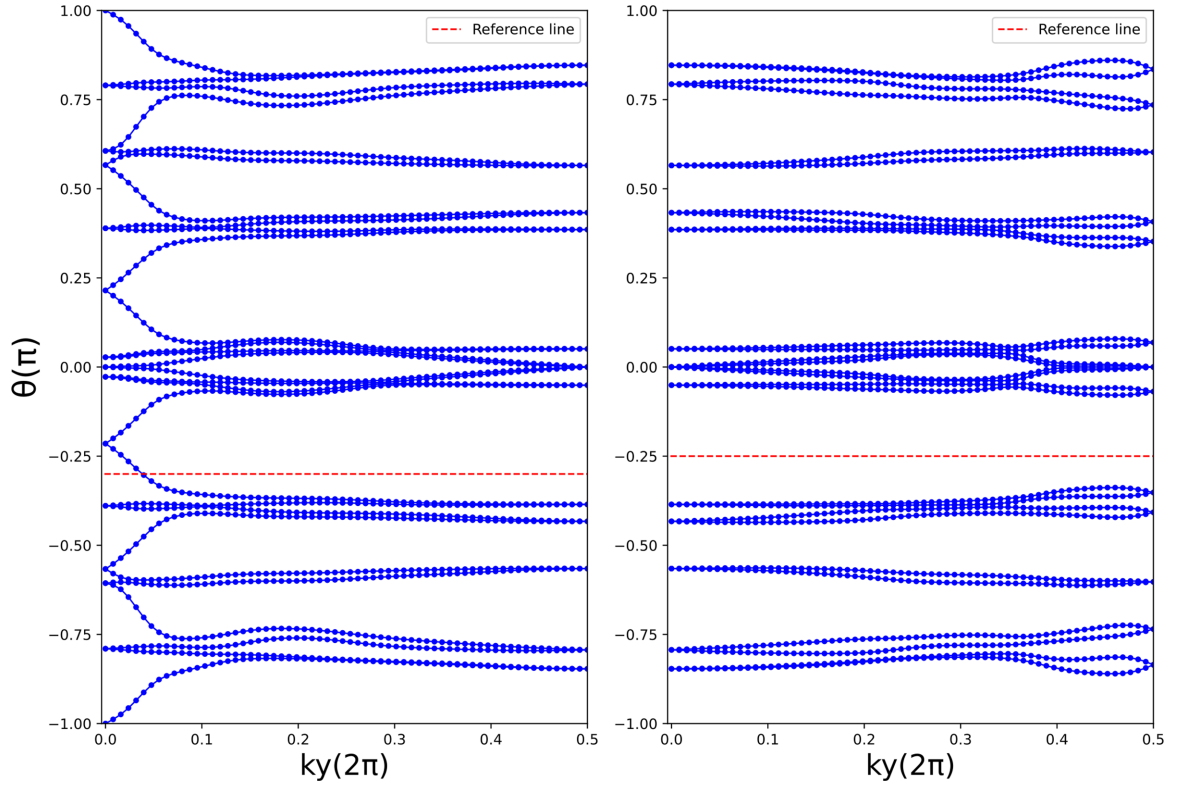


FIG. 9. Evolution of the Wannier charge center (WCC) in two different planes for an individual cluster, class $j = 34$, equivalent to pure Sb_2Se_3 . On the left graph $k_z = 0$ and on the right $k_z = 1$. The reference line (dashed red) crosses an odd number of times in the result of the plane with $k_z = 0$, which indicates that it is a material with a nontrivial topology.

IV. CONCLUSION

In summary, we combine the first principles calculations based on the DFT formalism with the statistical treatment

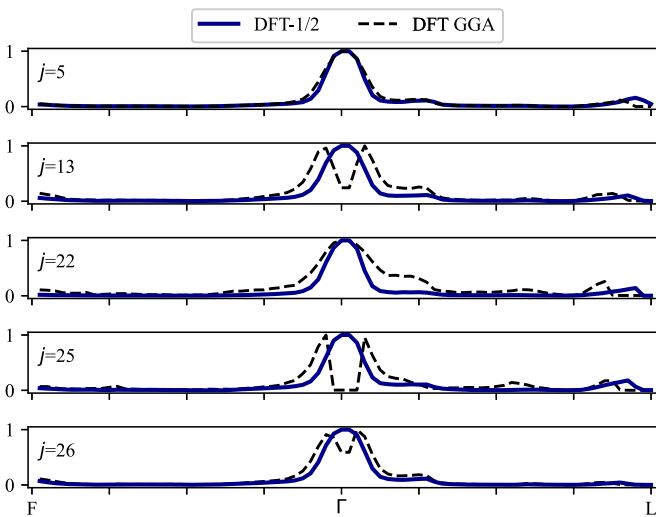


FIG. 10. Band inversion level $\eta_{\text{inv}}(\vec{k})$ calculated from Eq. (9) for five different cluster configurations. The results for the classes $j = 5, 13, 22, 25,$ and 26 are portrayed from the two methodologies of this work, DFT-1/2 (solid blue line) and DFT (dashed black line) in the path $F \leftarrow \Gamma \rightarrow L$.

provided by the GQCA to obtain reliable results from $(\text{Bi}_{1-x}\text{Sb}_x)_2\text{Se}_3$ topological alloys. The results of the topological invariant \mathbb{Z}_2 for all GQCA cluster configurations of the alloy indicate that there is a robustness of the properties and nontrivial topological character of the alloy along the entire composition range. The thermodynamic stability against composition phase separation of these systems is demonstrated.

An accurate and computationally cheap description of the electronic band structure is obtained by the application of the DFT-1/2 method. Our results indicate that the alloy has a maximum gap of 0.28 eV for an Sb concentration of $x = 0.70$ at $T = 300$ K, which is 60% larger than pure materials. Considering the isolated systems of individual clusters at temperature $T = 0$ K, the maximum energy gap E_{g_j} obtained through DFT-1/2 was 0.31 eV. These larger gaps in topological materials are desirable for technological applications at higher temperatures.

Our work proposes a combination of efficient *ab initio* calculations with approximated quasiparticle correction and a robust thermodynamic statistical approach for topological alloys. Its application on $(\text{Bi}_{1-x}\text{Sb}_x)_2\text{Se}_3$ provides experimentalists valuable information about how the energy gap can be chemically controlled, as well as the behavior of other physical properties along the entire chemical composition.

ACKNOWLEDGMENTS

This work was funded by the Brazilian agencies Conselho Nacional de Desenvolvimento Científico e Tecnológico (CNPq) (Grants No. 308742/2016-8, No. 306322/2017-0, and No. 316081/2023-0) and Coordenação de Aperfeiçoamento de Pessoal de Nível-Superior (CAPES) (Grants No.

88887.671852/2022-00). F.M. acknowledges support from Programa Unesp de Pós-Doutorado, Edital 13/2022. The authors also acknowledge the National Laboratory for Scientific Computing (LNCC/MCTI, Brazil) for providing HPC resources of the SDumont supercomputer and also the computational resources of the Laboratório de Computação Científica Avançada e Modelamento (LAB-CCAM).

- [1] M. Ali Shameli and L. Yousefi, Light trapping in thin film crystalline silicon solar cells using multi-scale photonic topological insulators, *Opt. Laser Technol.* **145**, 107457 (2022).
- [2] I. Caño, P. Vidal-Fuentes, A. G. Medaille, Z. Jehl, A. Jiménez-Argüjio, M. Guc, V. Izquierdo-Roca, C. Malerba, M. Valentini, M. Jiménez-Guerra, M. Placidi, J. Puigdollers, and E. Saucedo, Challenges and improvement pathways to develop quasi-1d $(\text{Sb}_{1-x}\text{Bi}_x)_2\text{Se}_3$ -based materials for optically tuneable photovoltaic applications. towards chalcogenide narrow-bandgap devices, *Sol. Energy Mater. Sol. Cells* **251**, 112150 (2023).
- [3] J. Zhang, C.-Z. Chang, Z. Zhang, J. Wen, X. Feng, K. Li, M. Liu, K. He, L. Wang, X. Chen, Q.-K. Xue, X. Ma, and Y. Wang, Band structure engineering in $(\text{Bi}_{1-x}\text{Sb}_x)_2\text{Te}_3$ ternary topological insulators, *Nat. Commun.* **2**, 574 (2011).
- [4] C. K. Barman and A. Alam, Topological phase transition in the ternary half-Heusler alloy ZrIrBi , *Phys. Rev. B* **97**, 075302 (2018).
- [5] N. Taghizade, G. Rashedi, Z. Nourbakhsh, and M. Farahi, Three-dimensional topological insulators of $\text{Cu}_x\text{Au}_{1-x}\text{InTe}_2$ alloys, *J. Alloys Compd.* **593**, 235 (2014).
- [6] Z. Nourbakhsh, Three-dimensional topological insulators of $\text{In}_2\text{Bi}_x\text{Sb}_{1-x}$ alloys, *J. Alloys Compd.* **549**, 51 (2013).
- [7] J. P. Heremans, R. J. Cava, and N. Samarth, Tetradymites as thermoelectrics and topological insulators, *Nat. Rev. Mater.* **2**, 17049 (2017).
- [8] Z. Ren, A. A. Taskin, S. Sasaki, K. Segawa, and Y. Ando, Large bulk resistivity and surface quantum oscillations in the topological insulator $\text{Bi}_2\text{Te}_2\text{Se}$, *Phys. Rev. B* **82**, 241306(R) (2010).
- [9] C. Niu, Y. Dai, Y. Zhu, Y. Ma, L. Yu, S. Han, and B. Huang, Realization of tunable dirac cone and insulating bulk states in topological insulators $(\text{Bi}_{1-x}\text{Sb}_x)_2\text{Te}_3$, *Sci. Rep.* **2**, 976 (2012).
- [10] Y. Pan, D. Wu, J. R. Angevaere, H. Luigjes, E. Frantzeskakis, N. de Jong, E. van Heumen, T. V. Bay, B. Zwartsenberg, Y. K. Huang, M. Snelder, A. Brinkman, M. S. Golden, and A. de Visser, Low carrier concentration crystals of the topological insulator $\text{Bi}_{2-x}\text{Sb}_x\text{Te}_{3-y}\text{Se}_y$: a magnetotransport study, *New J. Phys.* **16**, 123035 (2014).
- [11] J. Tang, L.-T. Chang, X. Kou, K. Murata, E. S. Choi, M. Lang, Y. Fan, Y. Jiang, M. Montazeri, W. Jiang, Y. Wang, L. He, and K. L. Wang, Electrical detection of spin-polarized surface states conduction in $(\text{Bi}_{0.53}\text{Sb}_{0.47})_2\text{Te}_3$ topological insulator, *Nano Lett.* **14**, 5423 (2014).
- [12] D. Hsieh, D. Qian, L. Wray, Y. Xia, Y. S. Hor, R. J. Cava, and M. Z. Hasan, A topological dirac insulator in a quantum spin hall phase, *Nature (London)* **452**, 970 (2008).
- [13] J. Liu and D. Vanderbilt, Topological phase transitions in $(\text{Bi}_{1-x}\text{In}_x)_2\text{Se}_3$ and $(\text{Bi}_{1-x}\text{Sb}_x)_2\text{Se}_3$, *Phys. Rev. B* **88**, 224202 (2013).
- [14] L. B. Abdalla, E. P. José, T. M. Schmidt, R. H. Miwa, and A. Fazzio, Topological phase transitions of $(\text{Bi}_x\text{Sb}_{1-x})_2\text{Se}_3$ alloys by density functional theory, *J. Phys.: Condens. Matter* **27**, 255501 (2015).
- [15] G. Cao, H. Liu, J. Liang, L. Cheng, D. Fan, and Z. Zhang, Rhombohedral Sb_2Se_3 as an intrinsic topological insulator due to strong van der waals interlayer coupling, *Phys. Rev. B* **97**, 075147 (2018).
- [16] R. Vadapoo, S. Krishnan, H. Yilmaz, and C. Marin, Electronic structure of antimony selenide (Sb_2Se_3) from gw calculations, *Phys. Status Solidi B* **248**, 700 (2011).
- [17] W. Li, X.-Y. Wei, J.-X. Zhu, C. S. Ting, and Y. Chen, Pressure-induced topological quantum phase transition in Sb_2Se_3 , *Phys. Rev. B* **89**, 035101 (2014).
- [18] W. Liu, X. Peng, C. Tang, L. Sun, K. Zhang, and J. Zhong, Anisotropic interactions and strain-induced topological phase transition in Sb_2Se_3 and Bi_2Se_3 , *Phys. Rev. B* **84**, 245105 (2011).
- [19] P. Hohenberg and W. Kohn, Inhomogeneous electron gas, *Phys. Rev.* **136**, B864 (1964).
- [20] W. Kohn and L. J. Sham, Self-consistent equations including exchange and correlation effects, *Phys. Rev.* **140**, A1133 (1965).
- [21] A.-B. Chen and A. Sher, *Semiconductor Alloys: Physics and Materials Engineering* (Plenum, New York, 1995).
- [22] L. K. Teles, J. Furthmüller, L. M. R. Scolfaro, J. R. Leite, and F. Bechstedt, First-principles calculations of the thermodynamic and structural properties of strained $\text{In}_x\text{Ga}_{1-x}\text{N}$ and $\text{Al}_x\text{Ga}_{1-x}\text{N}$ alloys, *Phys. Rev. B* **62**, 2475 (2000).
- [23] A. Sher, M. van Schilfgaarde, A.-B. Chen, and W. Chen, Quasi-chemical approximation in binary alloys, *Phys. Rev. B* **36**, 4279 (1987).
- [24] C. Caetano, L. K. Teles, M. Marques, A. Dal Pino, and L. G. Ferreira, Phase stability, chemical bonds, and gap bowing of $\text{In}_x\text{Ga}_{1-x}\text{N}$ alloys: Comparison between cubic and wurtzite structures, *Phys. Rev. B* **74**, 045215 (2006).
- [25] J. P. Perdew, Density functional theory and the band gap problem, *Int. J. Quantum Chem.* **28**, 497 (1985).
- [26] B. Yan, M. Jansen, and C. Felser, A large-energy-gap oxide topological insulator based on the superconductor BaBiO_3 , *Nat. Phys.* **9**, 709 (2013).
- [27] J. Vidal, X. Zhang, L. Yu, J.-W. Luo, and A. Zunger, False-positive and false-negative assignments of topological insulators in density functional theory and hybrids, *Phys. Rev. B* **84**, 041109(R) (2011).
- [28] S. X. Tao, X. Cao, and P. A. Bobbert, Accurate and efficient band gap predictions of metal halide perovskites using the dft-1/2 method: GW accuracy with DFT expense, *Sci. Rep.* **7**, 14386 (2017).

- [29] F. Matusalem, F. Bechstedt, I. Guilhon, M. Marques, and L. K. Teles, DFT-1/2 method applied to 2d topological insulators: fluorinated and hydrogenated group-IV honeycomb systems, *J. Phys.: Condens. Matter* **33**, 435501 (2021).
- [30] T. Mota, F. Matusalem, M. Marques, L. K. Teles, and I. Guilhon, DFT-1/2 method applied to 3d topological insulators, *J. Phys.: Condens. Matter* **34**, 465501 (2022).
- [31] L. G. Ferreira, M. Marques, and L. K. Teles, Approximation to density functional theory for the calculation of band gaps of semiconductors, *Phys. Rev. B* **78**, 125116 (2008).
- [32] L. G. Ferreira, M. Marques, and L. K. Teles, Slater half-occupation technique revisited: the LDA-1/2 and GGA-1/2 approaches for atomic ionization energies and band gaps in semiconductors, *AIP Adv.* **1**, 032119 (2011).
- [33] J. P. Perdew, K. Burke, and M. Ernzerhof, Generalized gradient approximation made simple, *Phys. Rev. Lett.* **77**, 3865 (1996).
- [34] P. E. Blöchl, Projector augmented-wave method, *Phys. Rev. B* **50**, 17953 (1994).
- [35] G. Kresse and D. Joubert, From ultrasoft pseudopotentials to the projector augmented-wave method, *Phys. Rev. B* **59**, 1758 (1999).
- [36] D. Gresch, G. Autès, O. V. Yazyev, M. Troyer, D. Vanderbilt, B. A. Bernevig, and A. A. Soluyanov, Z2pack: Numerical implementation of hybrid wannier centers for identifying topological materials, *Phys. Rev. B* **95**, 075146 (2017).
- [37] A. A. Soluyanov and D. Vanderbilt, Computing topological invariants without inversion symmetry, *Phys. Rev. B* **83**, 235401 (2011).
- [38] A. A. Mostofi, J. R. Yates, Y.-S. Lee, I. Souza, D. Vanderbilt, and N. Marzari, wannier90: A tool for obtaining maximally-localised wannier functions, *Comput. Phys. Commun.* **178**, 685 (2008).
- [39] N. Marzari and D. Vanderbilt, Maximally localized generalized wannier functions for composite energy bands, *Phys. Rev. B* **56**, 12847 (1997).
- [40] I. Souza, N. Marzari, and D. Vanderbilt, Maximally localized wannier functions for entangled energy bands, *Phys. Rev. B* **65**, 035109 (2001).
- [41] R. Yu, X. L. Qi, A. Bernevig, Z. Fang, and X. Dai, Equivalent expression of z_2 topological invariant for band insulators using the non-abelian berry connection, *Phys. Rev. B* **84**, 075119 (2011).
- [42] F. Matusalem, M. Marques, L. K. Teles, L. Matthes, J. Furthmüller, and F. Bechstedt, Quantization of spin hall conductivity in two-dimensional topological insulators versus symmetry and spin-orbit interaction, *Phys. Rev. B* **100**, 245430 (2019).
- [43] H. Zhang, C.-X. Liu, X.-L. Qi, X. Dai, Z. Fang, and S.-C. Zhang, Topological insulators in Bi_2Se_3 , Bi_2Te_3 and Sb_2Te_3 with a single dirac cone on the surface, *Nat. Phys.* **5**, 438 (2009).
- [44] I. Aguilera, C. Friedrich, and S. Blügel, Many-body corrected tight-binding hamiltonians for an accurate quasiparticle description of topological insulators of the Bi_2Se_3 family, *Phys. Rev. B* **100**, 155147 (2019).
- [45] Y. Satake, J. Shiogai, D. Takane, K. Yamada, K. Fujiwara, S. Souma, T. Sato, T. Takahashi, and A. Tsukazaki, Fermi-level tuning of the dirac surface state in $(\text{Bi}_{1-x}\text{Sb}_x)_2\text{Se}_3$ thin films, *J. Phys.: Condens. Matter* **30**, 085501 (2018).
- [46] A. V. Matetskiy, V. V. Mararov, I. A. Kibirev, A. V. Zotov, and A. A. Saranin, Trivial band topology of ultra-thin rhombohedral Sb_2Se_3 grown on Bi_2Se_3 , *J. Phys.: Condens. Matter* **32**, 165001 (2020).
- [47] Y. Liu, C. Chong, W. Chen, J.-A. Huang, C. Cheng, K. Tsuei, Z. Li, H. Qiu, and V. V. Marchenkov, Growth and characterization of mbe-grown $(\text{Bi}_{1-x}\text{Sb}_x)_2\text{Se}_3$ topological insulator, *Jpn. J. Appl. Phys.* **56**, 070311 (2017).
- [48] S. Nakajima, The crystal structure of $\text{Bi}_2\text{Te}_{3-x}\text{Se}_x$, *J. Phys. Chem. Solids* **24**, 479 (1963).
- [49] R. W. G. Wyckoff, *Crystal Structures* (Interscience, New York, 1964).
- [50] W. Liu, X. Peng, X. Wei, H. Yang, G. M. Stocks, and J. Zhong, Surface and substrate induced effects on thin films of the topological insulators Bi_2Se_3 and Bi_2Te_3 , *Phys. Rev. B* **87**, 205315 (2013).
- [51] T. Förster, P. Krüger, and M. Rohlfing, *Ab initio* studies of adatom- and vacancy-induced band bending in Bi_2Se_3 , *Phys. Rev. B* **91**, 035313 (2015).
- [52] S. Park and B. Ryu, Hybrid-density functional theory study on the band structures of tetradymite- Bi_2Te_3 , Sb_2Te_3 , Bi_2Se_3 , and Sb_2Se_3 thermoelectric materials, *J. Korean Phys. Soc.* **69**, 1683 (2016).
- [53] I. A. Nechaev, R. C. Hatch, M. Bianchi, D. Guan, C. Friedrich, I. Aguilera, J. L. Mi, B. B. Iversen, S. Blügel, P. Hofmann, and E. V. Chulkov, Evidence for a direct band gap in the topological insulator Bi_2Se_3 from theory and experiment, *Phys. Rev. B* **87**, 121111(R) (2013).
- [54] S. Chege, P. Ningi, J. Sifuna, and G. O. Amolo, Origin of band inversion in topological Bi_2Se_3 , *AIP Adv.* **10**, 095018 (2020).
- [55] M. Orlita, B. A. Piot, G. Martinez, N. K. S. Kumar, C. Faugeras, M. Potemski, C. Michel, E. M. Hankiewicz, T. Brauner, i. c. v. Drašar, S. Schreyeck, S. Grauer, K. Brunner, C. Gould, C. Brüne, and L. W. Molenkamp, Magneto-optics of massive dirac fermions in bulk Bi_2Se_3 , *Phys. Rev. Lett.* **114**, 186401 (2015).
- [56] O. V. Yazyev, E. Kioupakis, J. E. Moore, and S. G. Louie, Quasiparticle effects in the bulk and surface-state bands of Bi_2Se_3 and Bi_2Te_3 topological insulators, *Phys. Rev. B* **85**, 161101(R) (2012).
- [57] G. Martinez, B. A. Piot, M. Haki, M. Potemski, Y. S. Hor, A. Materna, S. G. Strzelecka, A. Hruban, O. Caha, J. Novák, A. Dubroka, Č. Drašar, and M. Orlita, Determination of the energy band gap of Bi_2Se_3 , *Sci. Rep.* **7**, 6891 (2017).
- [58] Y. L. Chen, J.-H. Chu, J. G. Analytis, Z. K. Liu, K. Igarashi, H.-H. Kuo, X. L. Qi, S. K. Mo, R. G. Moore, D. H. Lu, M. Hashimoto, T. Sasagawa, S. C. Zhang, I. R. Fisher, Z. Hussain, and Z. X. Shen, Massive dirac fermion on the surface of a magnetically doped topological insulator, *Science* **329**, 659 (2010).
- [59] P. Larson, V. A. Greanya, W. C. Tonjes, R. Liu, S. D. Mahanti, and C. G. Olson, Electronic structure of Bi_2X_3 ($X = \text{S}, \text{Se}, \text{T}$) compounds: Comparison of theoretical calculations with photoemission studies, *Phys. Rev. B* **65**, 085108 (2002).
- [60] J. Black, E. Conwell, L. Seigle, and C. Spencer, Electrical and optical properties of some $\text{M}_2^{\text{V}-\text{BN}}^{\text{VI}-\text{B}}$ semiconductors, *J. Phys. Chem. Solids* **2**, 240 (1957).
- [61] V. A. Greanya, W. C. Tonjes, R. Liu, C. G. Olson, D.-Y. Chung, and M. G. Kanatzidis, Determination of the valence band

- dispersions for Bi_2Se_3 using angle resolved photoemission, *J. Appl. Phys.* **92**, 6658 (2002).
- [62] E. Mooser and W. B. Pearson, New semiconducting compounds, *Phys. Rev.* **101**, 492 (1956).
- [63] S. K. Mishra, S. Satpathy, and O. Jepsen, Electronic structure and thermoelectric properties of bismuth telluride and bismuth selenide, *J. Phys.: Condens. Matter* **9**, 461 (1997).
- [64] D. Greenaway and G. Harbeke, Band structure of bismuth telluride, bismuth selenide and their respective alloys, *J. Phys. Chem. Solids* **26**, 1585 (1965).
- [65] G. Hyde, H. Beale, I. Spain, and J. Woollam, Electronic properties of Bi_2Se_3 crystals, *J. Phys. Chem. Solids* **35**, 1719 (1974).
- [66] See Supplemental Material at <http://link.aps.org/supplemental/10.1103/PhysRevB.109.235150> for complete results of the topological invariant of the 34 clusters and a comparison between results with and without spin-orbit interaction.
- [67] J. Liu and D. Vanderbilt, Spin-orbit spillage as a measure of band inversion in insulators, *Phys. Rev. B* **90**, 125133 (2014).